Nanofluidic Transport Governed by the Liquid-Vapour Interface

Jongho Lee[1], Tahar Laoui[2], and Rohit Karnik[1,]*

[1]*Department of Mechanical Engineering, Massachusetts Institute of Technology, 77 Massachusetts Avenue, Cambridge, MA 02139, USA.*

[2]*Department of Mechanical Engineering, King Fahd University of Petroleum and Minerals, Dhahran, Saudi Arabia.*

[*]*Corresponding author:*
Rohit Karnik
77 Massachusetts Ave., MIT Room 3-461A, Cambridge, MA 02139
Phone: 617-324-1155, Fax: 617-258-9346, Email: karnik@mit.edu

Abstract

Liquid-vapour interfaces govern the behaviour of a wide range of systems but remain poorly understood, leaving ample margin for the exploitation of intriguing functionalities for applications. Here we systematically investigate the role of liquid-vapour interfaces in the transport of water across apposing liquid menisci in osmosis membranes comprising short hydrophobic nanopores that separate two fluid reservoirs. We show experimentally that mass transport is limited by molecular reflection from the liquid-vapour interface below a certain length scale that depends on the transmission probability of water molecules across the nanopores and on the condensation probability of a water molecule incident on the liquid surface. This fundamental yet elusive condensation property of water is measured under near-equilibrium conditions and found to decrease from 0.36±0.21 at 30°C to 0.18±0.09 at 60°C. These findings define the regime in which liquid-vapour interfaces govern nanofluidic transport and have implications on understanding of mass

1

transport in nanofluidic devices, droplets and bubbles, biological components, and porous media involving liquid-vapour interfaces.

Transport of fluids through nanoscale conduits in nanofluidic devices and porous media is important in a variety of technological applications including biosensing[1,2], energy storage and conversion[3,4], biological and chemical separations[5,6], and water desalination[7]. While nanofluidic investigations have focused on solid-liquid interfacial phenomena such as surface charge-governed transport[8-10] and enormous slip lengths[11], two-phase flows involving liquid-vapour interfaces are readily found in nanofluidic environments including in capillary condensation, evaporation and cavitation in nanochannels[12,13], transport through hydrophobic membranes[14,15] and porous materials such as zeolites[16], as well as in the dynamics of nanoscale droplets and bubbles[17,18]. Liquid-vapour interfaces involve a phase transition and corresponding heat and mass transport resistances that are usually negligible in macroscopic systems[19], but can govern the behaviour of nanoscale systems.

In this article, we investigate the fundamental role of liquid-vapour interfaces in the transport of water across osmosis membranes wherein two liquid phases are separated by nanoscale vapour gaps. We show that interplay between mass transport in the vapour phase and that across the liquid-vapour interfaces leads to the emergence of a new length scale, below which mass transport is governed by molecular reflection at the liquid-vapour interface. This length scale is defined by a dimensionless parameter that has a probabilistic interpretation and depends critically on the condensation coefficient, a fundamental property of the fluid defining the probability with which a molecule incident from the vapour phase condenses on the liquid-vapour interface. We also measure the condensation coefficient of water under near-equilibrium conditions, which has thus far proved to be challenging. These results will be useful in the

2

understanding of nanofluidic phenomena involving liquid-vapour interfaces and in the design of nanofluidic systems and materials with two-phase flows.

Osmosis membranes with nanoscale vapour traps

To investigate the role of liquid-vapour interfaces in nanofluidic transport, we designed osmosis membranes comprising nanopores with short hydrophobic regions of tunable length that trap nanoscale pockets of vapour separating two liquid phases (Fig. 1a). Such membranes are also potentially useful for water desalination, where the nanoscale pockets of vapour are theoretically predicted to allow for selective transport of water under a mechanical or osmotic pressure difference while rejecting non-volatile solutes[15]. We fabricated the membranes starting with porous alumina with regular and controllable cylindrical nanopores that have found extensive use in nanofabrication[20,21]. The originally hydrophilic, ~70 nm diameter alumina nanopores were filled with photoresist and then plasma-etched to expose short lengths (200-2500 nm) of the nanopores (Fig. 1b). The exposed surface was modified with a hydrophobic self-assembled monolayer and the remaining photoresist was then dissolved, creating submicron-length hydrophobic nanopores embedded in the otherwise hydrophilic 50 μm-thick alumina membranes. The resulting membranes exhibited a hydrophobic top surface with a contact angle of 150.1±3.1° and hydrophilic bottom surface (Fig. 1c). The length and aspect ratio (AR = l/a, where l and a are pore length and radius, respectively) of the hydrophobic nanopores could be tuned by simply controlling the duration of the photoresist etching step (Fig. 1d-g), enabling control over the relative effect of the liquid-vapour interface on water transport as discussed later.

Several lines of evidence demonstrated the integrity of the fabricated membranes. After immersion in an aqueous gold nanoparticle solution, the particles were found to be excluded

from regions that were exposed for surface modification, consistent with exclusion of the liquid phase from the hydrophobic nanopores (Fig. 2a). Fig. 2a also suggests the creation of sharp two-phase interfaces co-located at the position to which the photoresist was originally etched. Over 90% of the nanopores had gold nanoparticles adsorbed up to the hydrophobic-hydrophilic boundaries, indicating good wetting of the hydrophilic surfaces. When two different fluorescent dye solutions were placed on either side of the membrane, confocal microscopy revealed that the solutions did not mix, although the gap between the two solutions was too small to be resolved (Fig. 2b). Environmental scanning electron microscopy under water vapour saturation conditions revealed that the top thin hydrophobic layer remained un-wetted (Fig. 2c). Finally, electrical conductance measurements showed that that only 0.1-1% of the nanopores were completely wetted (Supplementary Section S4).

Although aqueous solutions on both sides of the membrane are not directly connected, water can be transported across the membrane by evaporation and condensation. We verified vapour-phase transport by using a KCl solution to draw deionized water across the membrane by forward osmosis[22,23] (Fig. 3a). A circulating sheath flow of water was used to maintain uniform temperature, and the proximity of the two liquid-vapour interfaces combined with thermal conduction through alumina resulted in a negligible estimated temperature difference ($<10^{-4}$ °C). As expected, the flux of water increased with increasing osmotic pressure difference driving the flow, corresponding to increasing KCl concentration (Fig. 3b). Vapour-phase transport was further confirmed by adding a non-volatile dye to the deionized water side. UV-vis spectroscopy showed that the draw solution remained free of the dye even as water was transported across the membrane, corresponding to 99.90±0.025% rejection (Figure 3c, d; error indicates S.D. for three different membranes). With a nanopore diameter of 71.8±23.9 nm, point of zero charge of

4

alumina of about 8-9[24], and high KCl concentration (1 M), this exclusion cannot be attributed to electrostatic effects. In contrast, in the absence of hydrophobic modification the alumina membranes rapidly allowed salt and the dye to diffuse to the other side. These results confirm that water was transported as vapour-phase in the fabricated membranes, while non-volatile substances were rejected.

Effect of pore length on water transport

We investigated transport of water across membranes with different hydrophobic pore lengths using the same apparatus (Fig. 3a). The flux decreased monotonically with increasing pore length, corresponding to an increasing pore aspect ratio (Fig. 4a-c). For long pores, we expect the flux to vary inversely with the pore length, *i.e.* as AR^{-1}. While flux through the longer nanopores approaches this inverse scaling (solid line in Fig. 4c), the scaling breaks down for shorter nanopores, suggesting the emergence of different phenomena governing transport.

To understand this behaviour, we express the mass flux $\dot{m}$ across a membrane with porosity ε, considering the difference in evaporation rates at the two interfaces as the driving force across a series of transport resistances as follows:

$$\dot{m} = \varepsilon \frac{S_A\left(T_A, P_A, C_A\right) - S_B\left(T_B, P_B, C_B\right)}{\sum R}, \tag{1}$$

Here, S_A (or S_B) is the theoretical maximum evaporation rate from side A (or B), which equals the flux of impinging molecules from the vapour phase under equilibrium. It is directly related to the chemical potential of water and its equilibrium vapour pressure, P_{vap}, through the Hertz hypothesis[25], *i.e.*, $S_i = \sqrt{M/2\rho R_g T_i} P_{vap}\left(T_i, P_i, C_i\right)$ where M is the molar mass of water and R_g is the universal gas constant. The driving force $\Delta S = S_A - S_B$ therefore depends on the equilibrium

vapour pressure difference $P_{vap,A} - P_{vap,B}$ governed by temperature T, pressure drop P, and salt concentration C at each interface[15]. For isothermal, osmosis-driven flow, ΔS can be simplified as (see Supplementary Section 6)

$$S_A - S_B = \sqrt{\frac{MV_m^2}{2\rho R_g^3 T^3}}\left(P_{vap}^0(T)\mathrm{D}\mathrm{P}\right). \tag{2}$$

Here V_m is the molar volume of pure liquid water, $P^0{}_{vap}$ is the equilibrium vapour pressure of pure water with a flat interface, and $\Delta\Pi$ is the osmotic pressure difference ($\Delta\Pi = \Pi_B - \Pi_A$) driving the transport. Given that the liquid phases are at ambient pressure, any Laplace pressure drops across the menisci (<1 bar) cancel out and do not affect the flux of water.

$\Sigma R = R_t + 2R_i$ in Equation 1 denotes the resistance to transport, comprising i) a transmission resistance R_t associated with vapour-phase transmission of molecules across the nanopores; and ii) liquid-vapour interfacial resistances R_i associated with reflection of molecules at the liquid-vapour interfaces (Figure 4a). The hydrodynamic resistance to flow in the hydrophilic lengths of the nanopores is negligible.

$R_t = 1/\eta$, where η is the transmission probability of a gas molecule starting from one end of a pore to reach the other end[26]. R_t is dominated by collision of water molecules with pore walls in the Knudsen regime[27], but is influenced here to some extent by collisions with air molecules as the mean free path of water molecules in air (60-100 nm)[28] is comparable to the nanopore diameter. η monotonically decreases with AR, indicating an increasing probability of a molecule starting at one end to return to the same end before reaching the other end of the pore[29,30]. For pores with large AR, transport is described by a constant diffusion coefficient and scales as AR[-1]. In contrast, ballistic transport occurs in shorter nanopores causing deviation from the AR[-1]

6

relationship. However, the deviation observed in Figure 4c could also arise from the liquid-vapour interface that becomes significant for short nanopores (Fig. 4a).

R_i is governed by the probability that a water molecule impinging from the vapour phase condenses into the liquid phase, called condensation (or mass accommodation) coefficient[31]. Under thermodynamic equilibrium, it equals the evaporation coefficient defined as the flux ratio of molecules emitted (evaporated) from the liquid to that of molecules incident from the vapour phase[32]. In our experiments, the net flux is less than 2% of the flux of impinging molecules from the vapour phase. Therefore, we assume that the two coefficients are equal, denoted by σ. R_i is then defined as the ratio of the difference between the maximum evaporation rate and the net (sum of evaporated and reflected) mass flux leaving the interface, to the net mass flux across the interface, *i.e.*, $R_i = (1 - \sigma)/\sigma$ (see reference[15]).

Equation 2 explains the monotonic increase of flux with temperature for membranes with a fixed AR of 42.1±2.1 (Fig. 4d), since P^0_{vap} increases with temperature. The flux of water normalized by the driving force and membrane porosity (see Eqn. 1) depends only on transport resistance, *i.e.*, $\dot{m}/\epsilon DS = 1/\sum R$. We find that for membranes comprising longer nanopores (AR = 42.1±2.1) $\dot{m}/\epsilon DS$ is invariant with temperature (Fig. 4e). However, for membranes with short nanopores (AR = 9.6±0.7), $\dot{m}/\epsilon DS$ decreases with increasing temperature, indicating that $\Sigma R = R_t + 2R_i$ is temperature-dependent. While the transmission probability is only geometry dependent[26], the observed behaviour could reflect temperature dependence of σ as some studies suggest[33,34]. Any temperature dependence of R_i will only affect transport across shorter nanopores, as R_i becomes negligible compared to R_t for long pores. While these results suggest

7

that the liquid-vapour interface may play a role in the deviation from linearity observed in Figure 4c, we now turn our attention to clarify the magnitude of this effect.

Effect of interfacial resistance on water transport

To accurately quantify the contribution of the interfacial resistance to transport across the membrane, we included the effect of air molecules present in the nanopores. We derived a modified transmission probability (η_{eff}) using the dusty-gas model that is widely employed for gas flow through porous media[35-37]. The model accounts for interaction among gas molecules as well with the pore wall, and has been experimentally verified for binary[38] and ternary[39] gas mixtures under conditions varying from Knudsen to viscous regimes. η_{eff} is given by (see Supplementary Section 7 for derivation):

$$\frac{1}{h_{eff}} = \frac{1}{h} + \frac{\left(1 - P_{vap}^0 / p\right)\overline{u}l}{4D_{wa}},$$ (3)

where D_{wa} is binary diffusion coefficient of vapour in air, $\overline{u}$ is the mean speed of water molecules in vapour phase, and η is the transmission probability in the Knudsen regime. p indicates the total pressure (≤1 bar) inside the nanopores that was estimated as 0.5±0.3 bar by measuring oxygen concentration in the solution (See Supplementary Sections 2 & 9). Equation 3 shows that the presence of air molecules at 1 bar decreases the transmission probability by ~35% for the nanopore geometry considered here (Supplementary Fig. 5). The flux of water can now be written in terms of η_{eff} :

$$\frac{\dot{m}}{eDS} = \frac{1}{R_t + 2R_i} = \frac{1}{\dfrac{1}{h_{eff}} + \dfrac{2(1 - s)}{s}}.$$ (4)

To isolate the effect of the condensation coefficient, we normalized the flux by that expected for a condensation coefficient of unity (*i.e.* $R_i = 0$, Fig. 5a). We find that the normalized flux approaches unity for large AR (longer pores) where we expect the liquid-vapour interfaces to offer minimal resistance, verifying that Equation 4 (which does not have any fitting parameters when R_i is negligible) accurately accounts for the transmission resistance. However, for small AR the mass flux is significantly lower than that predicted for zero interfacial resistance, indicating a condensation coefficient less than unity and a significant contribution of the interfacial resistance to transport.

The results demonstrate the existence of two transport regimes: The first regime occurs in large AR pores in which the influence of condensation coefficient (and therefore interfacial resistance) is negligible and mass flux is governed by the transmission resistance. The second regime corresponds to small AR pores where the interfacial resistance is significant. The two regimes are delineated by a dimensionless parameter $\psi \equiv R_i/R_t = \eta_{\text{eff}}\,(1 - \sigma)/\sigma$, given by the ratio of the interfacial and transmission resistances. The effect of the liquid-vapour interface becomes significant when ψ increases (Fig. 5a,b). ψ has an interesting probabilistic interpretation. When the interfacial resistance is negligible, the outward flux of molecules evaporated from the interface must be S_A. This flux constitutes molecules that have directly evaporated, and those that have returned with probability $r = (1 - \eta_{\text{eff}})$ and have been reflected from the meniscus with probability $(1 - \sigma)$. Considering one meniscus and assuming that the other is ideal ($\sigma = 1$), the outward flux from the first meniscus is simply given by

$\sigma S_A \left(1 + r(1 - \sigma) + r^2 (1 - \sigma)^2 + ... \right) = S_A /(1 + \psi)$. Hence, $\psi \ll 1$ is the condition for the outward flux from the meniscus to approach that for an ideal meniscus. When $\sigma = 1$, the directly evaporated flux equals the ideal flux and there is no contribution from reflection, but when $\sigma < 1$, a finite

9

return probability (*i.e.* $\eta_{\text{eff}} < 1$) combined with reflection from the meniscus ensures a close to ideal flux if $y \ll 1$. Conversely, if we consider molecules incident on the meniscus, for $y \ll 1$ molecules impinging on the meniscus either readily condense upon incidence when $\sigma = 1$, or if they are reflected when $\sigma < 1$, they always return back to the meniscus ($\eta_{\text{eff}} \ll 1$) and condense. On the other hand, for $y \gg 1$, impinging molecules cannot readily condense upon incidence ($\sigma \ll 1$), or the reflected molecules ($\sigma < 1$) escape to the other side readily ($\eta_{\text{eff}} \approx 1$) so that the chance of condensation on the meniscus is small.

While the interface can govern transport of water, the membrane permeance $\dot{m}/\text{DP}$ measured in this study (see Fig. 4c) for porosity ~10% is comparable to that of polyamide-based forward osmosis membranes (~6.7×10^{-5} kg/m^{2}s-bar)[40], which is ~10^3-fold smaller than Poiseuille flow through the unmodified membrane. However, vapour-phase transport provides high selectivity for non-volatile substances while potentially retaining flexibility in the choice of membrane material for improving properties such as chemical resistance.

Condensation coefficient of water

The experiments also enable estimation of the condensation coefficient (σ) of water, which has been the subject of long debates and disagreements for nearly a century (See Supplementary Section 8). The difficulty in accurately measuring σ arises from uncertainties in estimating heat and mass transfer resistances and the interfacial temperature in the presence of latent heat transfer[41-43], since vapour pressure is a strong function of temperature. As a result, experimental estimates even in relatively recent studies (since 1989) are scattered over almost two orders of magnitude (0.01 to 1)[31,34,44-47]. Molecular dynamics simulations have also yielded varying values depending on the models used[48,49]. In the experiments reported here, the transport resistance is

measured under nearly isothermal conditions ($\Delta T_{max} < 10^{-4}$ °C). Control of the nanopore

geometry also allows for accurate estimation of the mass transport resistance, as verified by

excellent agreement of Equation 4 with data in the case of membranes with large AR (Fig. 5a).

We find that a condensation coefficient of 0.23 describes the experimental results at 39.0°C for

the entire range of AR (dashed line in Fig. 5a). The condensation coefficients estimated at each

AR at 39.0°C agree for the small AR pores, while the uncertainties are large at higher AR where

the interfacial resistance has a minimal impact on transport (Fig. 5c). Condensation coefficients

estimated at different temperatures for AR = 9.6±0.7 show a decreasing trend (Fig. 5d), which

qualitatively agrees with a recent experimental study[34]. This study carefully minimized

temperature gradients by tracing the condensation of $H_2^{17}O$ on water droplets injected into

vapour at high speeds, although at temperatures below 7 °C and at speeds corresponding to a

vapour temperature elevated by ~10-50 K. Interestingly, the condensation coefficients match

with those in the present work if the temperature scale is shifted by ~40 K. The experiments

reported here overcome many of the major uncertainties involved in measurement of the

condensation coefficient, and demonstrate that majority of water molecules incident on the

liquid-vapour interface are reflected back into the vapour phase. Although the condensation

coefficient measured here is strictly speaking an averaged value of that at the two interfaces, the

absence of significant dependence on salt concentration, or the type of anion (Cl^- was switched

with I^- that tends to accumulate at the interface[50] as described in Supplementary Section 11)

leads to the conclusion that the measured condensation coefficient is quite close to that of pure

water.

Conclusion

In summary, we investigated the transport of water across short hydrophobic nanopores flanked by liquid-vapour interfaces. We fabricated osmosis membranes consisting of hydrophobic nanopores with tunable lengths, and verified vapour-phase transport across the membranes. Measurements of the osmotic flow of water for different pore aspect ratios, osmotic pressures, and temperatures demonstrate the existence of a mass transport regime governed by resistance of the liquid-vapour interface, which is determined by interplay between the condensation coefficient of water and the mass transfer resistance across the pores. We estimated the magnitude of the condensation coefficient of water at different temperatures under isothermal conditions, and found that it decreases with increasing temperature. These findings would lead to better understanding and prediction of mass transfer through nanofluidic devices, droplets and bubbles, biological components with two-phase interfaces, and porous media.

Methods

See Supplementary information for detailed methods and theoretical analysis.

Fabrication

Porous alumina membranes (1cm x 1cm, Synkera Technology Inc.) with nominal diameter of 100 nm (actual diameter: 71.8±23.9 nm) were annealed at 1,000 °C to transform the material from alumite to γ-alumina to prevent dissolution in water during the experiments (See Supplementary Section 1). Positive photoresist AZ 5214E was placed under vacuum for 16 h to reduce the solvent content. The membranes were placed on a droplet (~7 μL) of the photoresist for 2 h to fill the nanopores and then baked on a hot plate at 100 °C for 50 min to evaporate the solvent. The photoresist was then etched by air plasma in a plasma cleaner (Harrick Plasma Inc.)

at 7.16 W and ~0.7 mTorr. The membranes were then briefly washed with an aqueous solution of 5wt% phosphoric acid for about 1 min, dried with nitrogen, and exposed to vapour of perfluorodecyltrichlorosilane (Gelest) overnight in a vacuum desiccator. After majority of the photoresist was removed by washing in acetone, both sides of the membranes were exposed to UV light (~200 W) for 4 min each and the membrane was immersed in 3v/v% aqueous solution of ammonium hydroxide for 30 min to remove photoresist residues. The membranes were then baked overnight at 90 °C. Additional fabrication details are provided in Supplementary Section 1.

Membrane characterization and calculation of flux

For flux measurement, batches of 6 − 10 membranes for each AR were fabricated. Membrane porosity was estimated by SEM imaging of randomly selected membranes. Assuming straight nanopores, the portion of area taken by nanopores on the top surface SEM images is regarded as porosity and was calculated by ImageJ software. Effective diameters of the individual nanopores were calculated by assuming circular pore shape having the same cross-section area of each nanopore. The average porosity and nanopores diameter were 9.88±2.13% and 71.8±23.9 nm, respectively. To obtain the average AR, a reference membrane was selected from each batch after plasma etching step and was cleaved to image the cross-section of the membrane by SEM (see Fig. 1d) and the etch depth was measured at 5 − 10 different locations. The distribution of the etch depths and the pore diameters was used to calculate the AR distribution (Fig. 1f). For flux calculation, sets of ARs were constructed by taking each etch depth divided by the individual nanopore radii measured using SEM. For each set of the ARs corresponding to each etch depth, an equivalent flux-averaged AR was obtained. Finally, the average of such equivalent ARs was regarded as the average AR for each membrane batch (see Supplementary Section 3). The defect rate (portion of hydrophilic or wetted nanopores) in the membranes was calculated

based on impedance measurement across the membranes (See Supplementary Section 4) and was less than 1% in all cases.

Measurement of osmotic flux

The membrane was mounted between diffusion cells (Permegear Inc.) with 7 mL volumes on each side of the membrane. A graduated 250-µL glass syringe (Hamilton Co.) was mounted on the cell containing the draw solution to measure the volume change. Before each forward osmosis experiment, the cells were cleaned with piranha solution and by sonication for 1 h. A camera was set up to acquire images of the syringe at designated time intervals, from which the volume change was analysed by Photoshop software. A constant temperature sheath flow around the cells was maintained using a peristaltic pump that circulated water from an external temperature-controlled water bath. The hydrophobic side of the membrane was always mounted facing the draw solution to ensure minimal concentration polarization. In all experiments, solute concentration on the hydrophilic side was low enough to ensure that concentration polarization was negligible.

References

1. Vlassiouk, I., Kozel, T. & Siwy, Z. Biosensing with Nanofluidic Diodes. *J. Am. Chem. Soc*. **131**, 8211-8220 (2009).

2. Fan, R. et al. DNA translocation in inorganic nanotubes. *Nano Lett*. **5**, 1633-1637 (2005).

3. Siria, A. et al. Giant osmotic energy conversion measured in a single transmembrane boron nitride nanotube. *Nature* **494**, 455-458 (2013).

4. Brogioli, D. Extracting Renewable Energy from a Salinity Difference Using a Capacitor. *Phys. Rev. Lett*. **103**, 058501 (2009).

5.   Han, J. & Craighead, H. Separation of long DNA molecules in a microfabricated entropic trap array. *Science* **288**, 1026-1029 (2000).

6.   Zeng, Y. & Harrison, D. Self-assembled colloidal arrays as three-dimensional nanofluidic sieves for separation of biomolecules on microchips. *Anal. Chem.* **79**, 2289-2295 (2007).

7.   Kim, S., Ko, S., Kang, K. & Han, J. Direct seawater desalination by ion concentration polarization. *Nature Nanotech.* **5**, 297-301 (2010).

8.   Karnik, R. et al. Electrostatic control of ions and molecules in nanofluidic transistors. *Nano Lett.* **5**, 943-948 (2005).

9.   Vlassiouk, I. & Siwy, Z. Nanofluidic diode. *Nano Lett.* **7**, 552-556 (2007).

10.   Wang, Y., Stevens, A. & Han, J. Million-fold preconcentration of proteins and peptides by nanofluidic filter. *Anal. Chem.* **77**, 4293-4299 (2005).

11.   Holt, J. et al. Fast mass transport through sub-2-nanometer carbon nanotubes. *Science* **312**, 1034-1037 (2006).

12.   Tas, N., Mela, P., Kramer, T., Berenschot, J. & van den Berg, A. Capillarity induced negative pressure of water plugs in nanochannels. *Nano Lett.* **3**, 1537-1540 (2003).

13.   Duan, C., Karnik, R., Lu, M. & Majumdar, A. Evaporation-induced cavitation in nanofluidic channels. *Proc. Natl Acad. Sci.* **109**, 3688-3693 (2012).

14.   Lawson, K. & Lloyd, D. Membrane distillation. *J. Membr. Sci.* **124**, 1-25 (1997).

15.   Lee, J. & Karnik, R. Desalination-of water by vapor-phase transport through hydrophobic nanopores. *J. Appl. Phys.* **108**, 044315 (2010).

16.   Cailliez, F., Stirnemann, G., Boutin, A., Demachy, I. & Fuchs, A. Does water condense in hydrophobic cavities? A molecular simulation study of hydration in heterogeneous nanopores. *J. Phys. Chem. C* **112**, 10435-10445 (2008).

17.   James, M. et al. Nanoscale condensation of water on self-assembled monolayers. *Soft Matter* **7**, 5309-5318 (2011).

18.   Tyrrell, J. & Attard, P. Images of nanobubbles on hydrophobic surfaces and their interactions. *Phys. Rev. Lett.* **87**, 176104 (2001).

19.   Qu, X. & Davis, E. Droplet evaporation and condensation in the near-continuum regime. *J. Aerosol Sci.* **32**, 861-875 (2001).

20.   Xiao, Z. et al. Fabrication of alumina nanotubes and nanowires by etching porous alumina membranes. *Nano Lett.* **2**, 1293-1297 (2002).

21.   Yanagishita, T., Nishio, K. & Masuda, H. Fabrication of metal nanohole arrays with high aspect ratios using two-step replication of anodic porous alumina. *Adv. Mater.* **17**, 2241-2243 (2005).

22.   Cath, T., Childress, A. & Elimelech, M. Forward osmosis: Principles, applications, and recent developments. *J. Membr. Sci.* **281**, 70-87 (2006).

23.   Gryta, M. Osmotic MD and other membrane distillation variants. *J. Membr. Sci.* **246**, 145-156 (2005).

24.   Yan, R., Liang, W., Fan, R. & Yang, P. Nanofluidic Diodes Based on Nanotube Heterojunctions. *Nano Lett.* **9**, 3820-3825 (2009).

25.   Eames, I., Marr, N. & Sabir, H. The evaporation coefficient of water: A review. *Int. J. Heat Mass Trans.* **40**, 2963-2973 (1997).

26.   Clausing, P. Flow of Highly Rarefied Gases Through Tubes of Arbitrary Length. *J. Vac. Sci. Technol.* **8**, 636-646 (1971).

27.   Cunningham, R.E. & Williams, R.J.J. *Diffusion in gases and porous media*. (Plenum Press, New York; 1980).

28.   Chapman, S., Cowling, T.G. & Burnett, D. *The mathematical theory of non-uniform gases; an account of the kinetic theory of viscosity, thermal conduction and diffusion in gases, Edn. 3rd.* (Cambridge University Press, Cambridge, Eng.; 1970).

29.   Demarcus, W. & Hopper, E. Knudsen Flow Through a Circular Capillary. *J. Chem. Phys.* **23**, 1344-1344 (1955).

30.   Berman, A. Free Molecule Transmission Probabilities. *J. Appl. Phys.* **36**, 3356 (1965).

31.   Winkler, P. et al. Mass and thermal accommodation during gas-liquid condensation of water. *Phys. Rev. Lett.* **93**, 075701 (2004).

32.   Marek, R. & Straub, J. Analysis of the evaporation coefficient and the condensation coefficient of water. *Int. J. Heat Mass Trans.* **44**, 39-53 (2001).

33.   Delaney, L., Houston, R. & Eagleton, L. The Rate of Vaporization of Water and Ice. *Chem. Eng. Sci.* **19**, 105-114 (1964).

34.   Li, Y. et al. Mass and thermal accommodation coefficients of H2O(g) on liquid water as a function of temperature. *J. Phys. Chem. A* **105**, 10627-10634 (2001).

35.   Mason, E.A. & Malinauskas, A.P. *Gas transport in porous media: the dusty-gas model*. (Elsevier, Amsterdam ; New York; 1983).

36.   Jackson, R. *Transport in porous catalysts*. (Elsevier Scientific Pub. Co., Amsterdam ; New York; 1977).

37.   Krishna, R. & Wesselingh, J. Review article number 50 - The Maxwell-Stefan approach to mass transfer. *Chem. Eng. Sci.* **52**, 861-911 (1997).

38.   Remick, R. & Geankoplis. C.J. Binary Diffusion of Gases in Capillaries in the Transition Region between Knudsen and Molecular Diffusion. *Ind. Eng. Chem. Fundam.* **12**, 214-220 (1973).

39.   Remick, R. & Geankoplis. C.J. Ternary Diffusion of Gases in Capillaries in the Transition Region between Knudsen and Molecular Diffusion. *Chem. Eng. Sci.* **29**, 1447-1455 (1974).

40.   Yip, N., Tiraferri, A., Phillip, W., Schiffman, J. & Elimelech, M. High Performance Thin-Film Composite Forward Osmosis Membrane. *Environ. Sci. Technol.* **44**, 3812-3818 (2010).

41.   Bonacci, J., Myers, A., Nongbri, G. & Eagleton, L. The evaporation and condensation coefficient of water, ice and carbon tetrachloride. *Chem. Eng. Sci.* **31**, 609-617 (1976).

42.   Mills, A. & Seban, R. Condensation Coefficient of Water. *Int. J. Heat Mass Trans.* **10**, 1815-1827 (1967).

43.   Mozurkewich, M. Aerosol Growth and the Condensation Coefficient for Water: A Review. *Aerosol Sci. Technol.* **5**, 223-236 (1986).

44.   Hagen, D. et al. Condensation Coefficient Measurement for Water in the UMR Cloud Simulation

        Chamber. *J. Atmos. Sci.* **46**, 803-816 (1989).

45.   Maerefat, M., Akamatsu, T. & Fujikawa, S. Non-equilibrium condensation of water and

        carbontetrachloride vapour in a shock-tube. *Exp. Fluids* **9**, 345-351 (1990).

46.   Shaw, R. & Lamb, D. Experimental determination of the thermal accommodation and

        condensation coefficients of water. *J. Chem. Phys.* **111**, 10659-10663 (1999).

47.   Davidovits, P. et al. Mass accommodation coefficient of water vapor on liquid water. *Geophys.*

        Res. Lett. **31**, L22111 (2004).

48.   Ishiyama, T., Yano, T. & Fujikawa, S. Molecular dynamics study of kinetic boundary condition

        at an interface between a polyatomic vapor and its condensed phase. *Phys. Fluids* **16**, 4713-4726

        (2004).

49.   Meland, R., Frezzotti, A., Ytrehus, T. & Hafskjold, B. Nonequilibrium molecular-dynamics

        simulation of net evaporation and net condensation, and evaluation of the gas-kinetic boundary

        condition at the interphase. *Phys. Fluids* **16**, 223-243 (2004).

50.   Jungwirth, P. & Tobias, D. Specific ion effects at the air/water interface. *Chem. Rev.* **106**, 1259-

        1281 (2006).

Acknowledgements

Author Contributions

J. L. and R. K. conceived and designed the experiments. J. L. performed the research. J. L., T. L., and R. K. analysed the data and discussed the results. J. L. and R. K. wrote the manuscript.

Additional Information

Supplementary information accompanies this paper at www.nature.com/naturenanotechnology. Reprints and permission information is available online at http://npg.nature.com/reprintsandpermissions/. Correspondence and requests for materials should be addressed to R. K.

Competing Financial Interests

The authors declare no completing financial interests.

Figure Legends
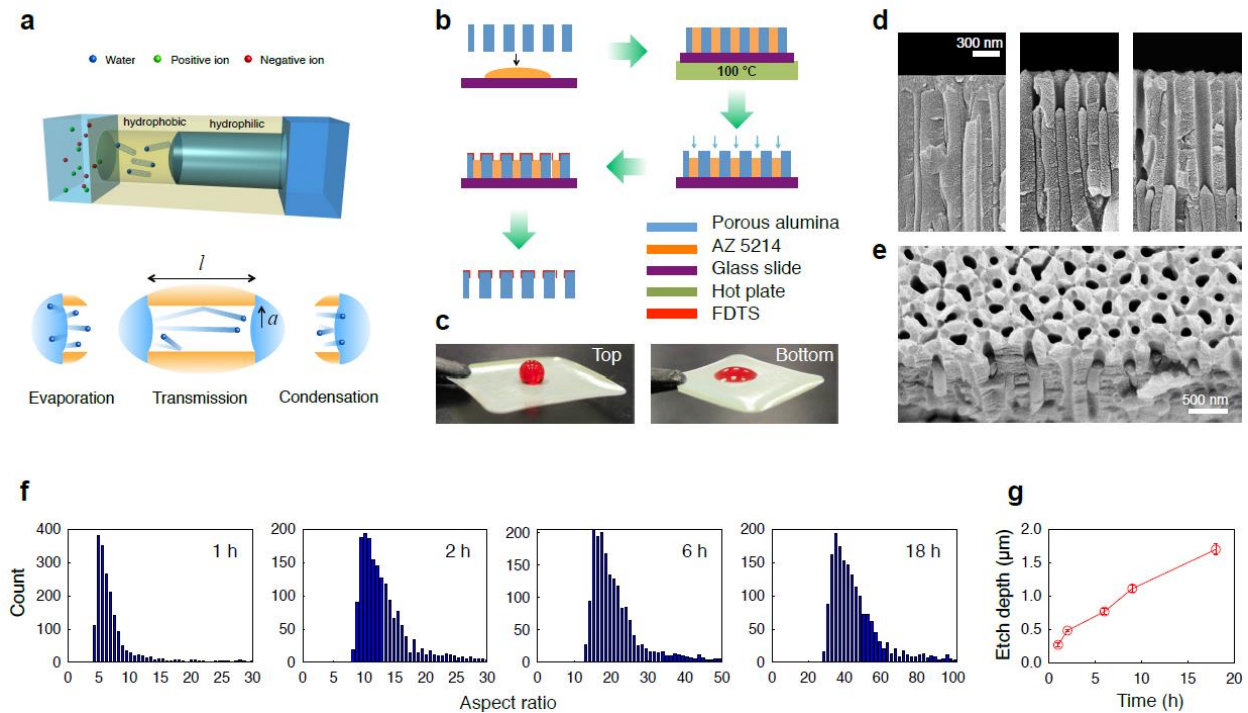
Figure 1. Fabrication of osmosis membranes with nanoscale vapour traps. a, Schematic illustration of membrane with short hydrophobic nanopores that trap vapour. **b**, Schematic of fabrication processes. i) porous alumina membrane soaked with photoresist AZ5214, ii) solvent evaporation on hot plate, iii) air plasma treatment for photoresist etching, iv) silanization on exposed alumina surface with perfluorodecyltrichlorosilane (FDTS), v) removal of residual photoresist. **c**, The fabricated membranes have a hydrophobic top surface (left) and hydrophilic bottom surface (right). **d**, SEM images of cross-section of nanopores after no plasma treatment (left), 2 h (middle), 9 h (right) of treatment, illustrating control of pore length for hydrophobic modification. Scale bar is 300 nm. **e**, SEM image of membrane after 2 h plasma treatment. Scale bar is 500 nm. **f**, Aspect ratio (AR) distribution of nanopores after plasma treatment for different

time periods. **g**, Photoresist etch depth for different plasma treatment periods. Error bars

represent ±S.D.
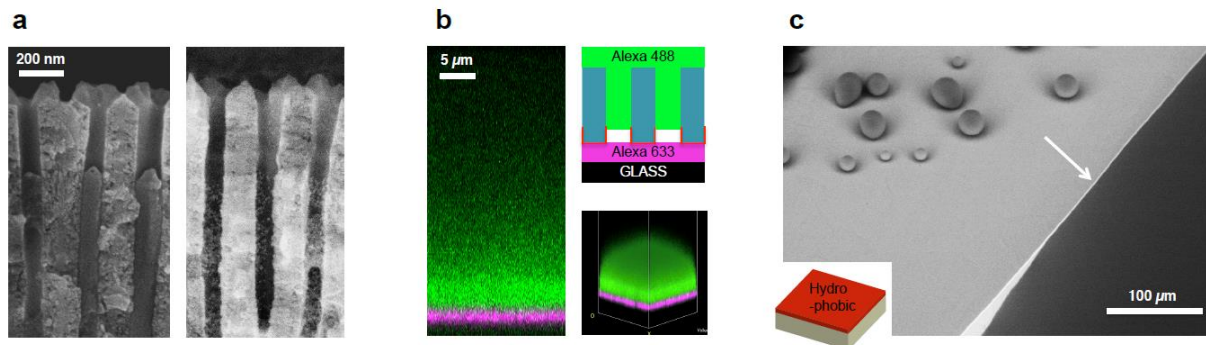

Figure 2. Verification of membrane integrity. a, SEM images of cross-section of nanopores

after 2 h plasma treatment (left) and after immersion of the fabricated membrane in 3 nm gold

nanoparticle solution (right) show co-localization of the nanoparticles with the extent of

photoresist etching. Scale bar is 200 nm. **b**, Confocal microscopy of the membrane exposed to

two different fluorescence dye solutions (Alexa 633 and Alexa 488 in deionized water) on either

sides of membrane reveals a distinct interface with lack of mixing. Scale bar is 5 μm. **c**,

Environmental SEM image of fabricated membrane showing hydrophilic and hydrophobic

surfaces. Arrow indicates the non-wetted region appearing as a thin line corresponding to the

hydrophobic modification. Scale bar is 100 μm.
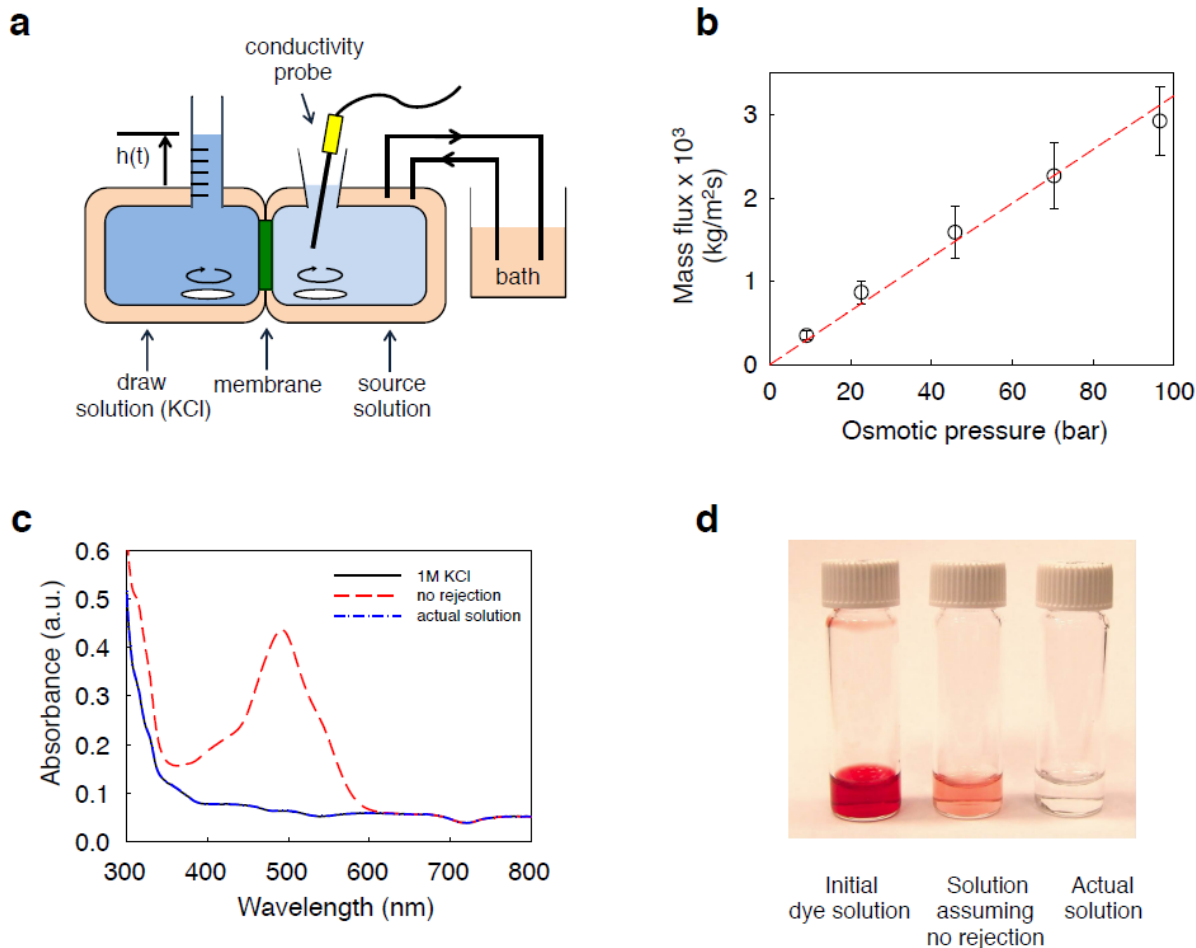
Figure 3. Demonstration of vapour-phase transport. a, Schematic diagram of diffusion cells with draw solution (KCl) and deionized water. Magnetic stir bars enhance mixing of solutions and minimize concentration polarization. **b**, Measured mass flux through a membrane for different osmotic pressure differences using 0.2, 0.5, 1, 1.5, and 2 M KCl as draw solutions, at a temperature of 25°C. Red dotted line is drawn as a guide for the eyes. Error bars represent ±S.D. for three different measurements on one membrane. **c**, UV-vis spectra show rejection of Allura Red dye. Black, 1 M KCl solution; red, Allura Red solution in 1 M KCl assuming zero rejection of dye mimicking how the draw solution would look if water were transported without dye rejection; blue, actual draw solution. **d**, 2 mM Allura Red solution in deionized water drawn across the membrane by the draw solution (left), Allura Red solution in 1 M KCl assuming zero

rejection of dye mimicking how the draw solution would look if water were transported without

dye rejection (middle), actual solution in draw solution cell after experiment showing dye
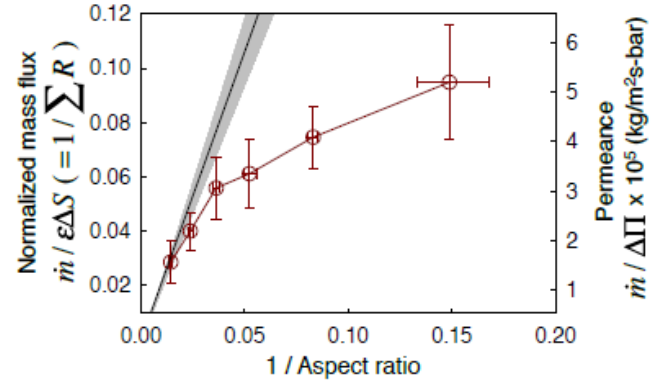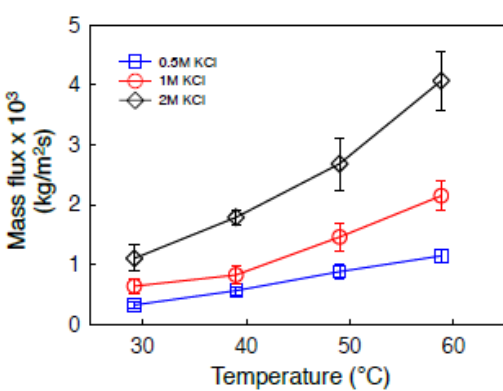
rejection (right).
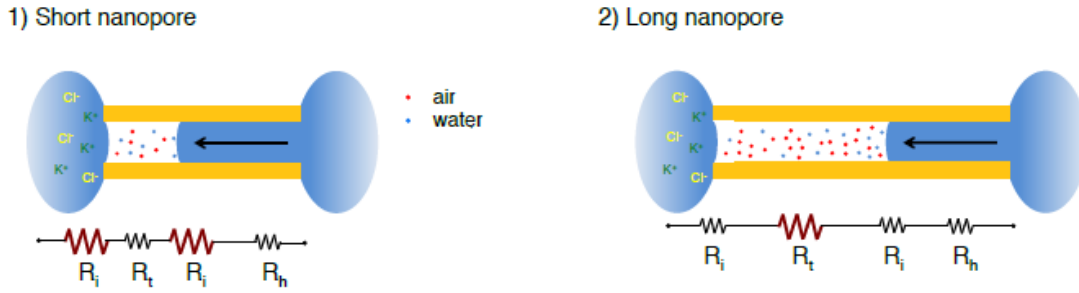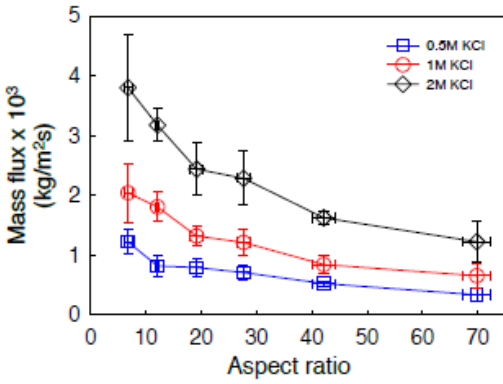
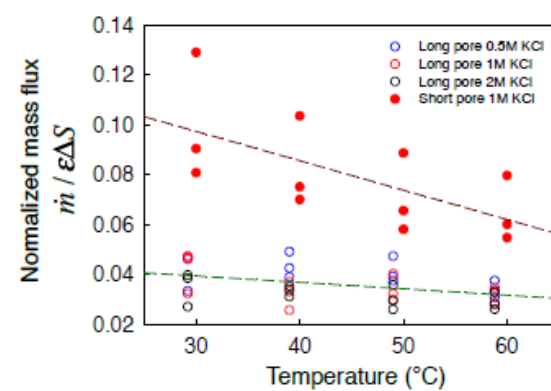**Figure 4. Scaling behaviour of the measured water flux. a**, Schematic of resistance models for

"short" and "long" nanopores. R_i, interfacial resistance; R_t, transmission resistance; R_h,

hydrodynamic resistance. **b**, Variation of mass flux with AR for different KCl concentrations of

draw solution measured at 39.0±0.3°C. **c**, Scaling of the measured mass flux normalized by maximum flux $(S_A - S_B)$ with AR^{-1}. Note that as AR decreases, the normalized flux deviates from the solid line 2.12/AR corresponding to an inverse scaling expected in the case of long pores, plotted for pressure inside nanopore, p, of 0.5 bar. The shaded area indicates the possible range corresponding to $0.2 \leq p \leq 0.8$ bar (See Supplementary Section 10). **d**, Dependence of the

measured mass flux on temperature for AR = 42.1±2.1. **e**, Temperature dependence of total resistance for "long" pores with AR of 42.1±2.1 and for "short" pores with AR of 9.6±0.7. Dotted lines are linear fits to data averages to guide the eyes. Vertical error bars in all panels represent ±S.D. corresponding to measurements on 3 to 5 different membranes for each data point. Horizontal error bars in all panels represent ±S.D. for AR as described in Methods.
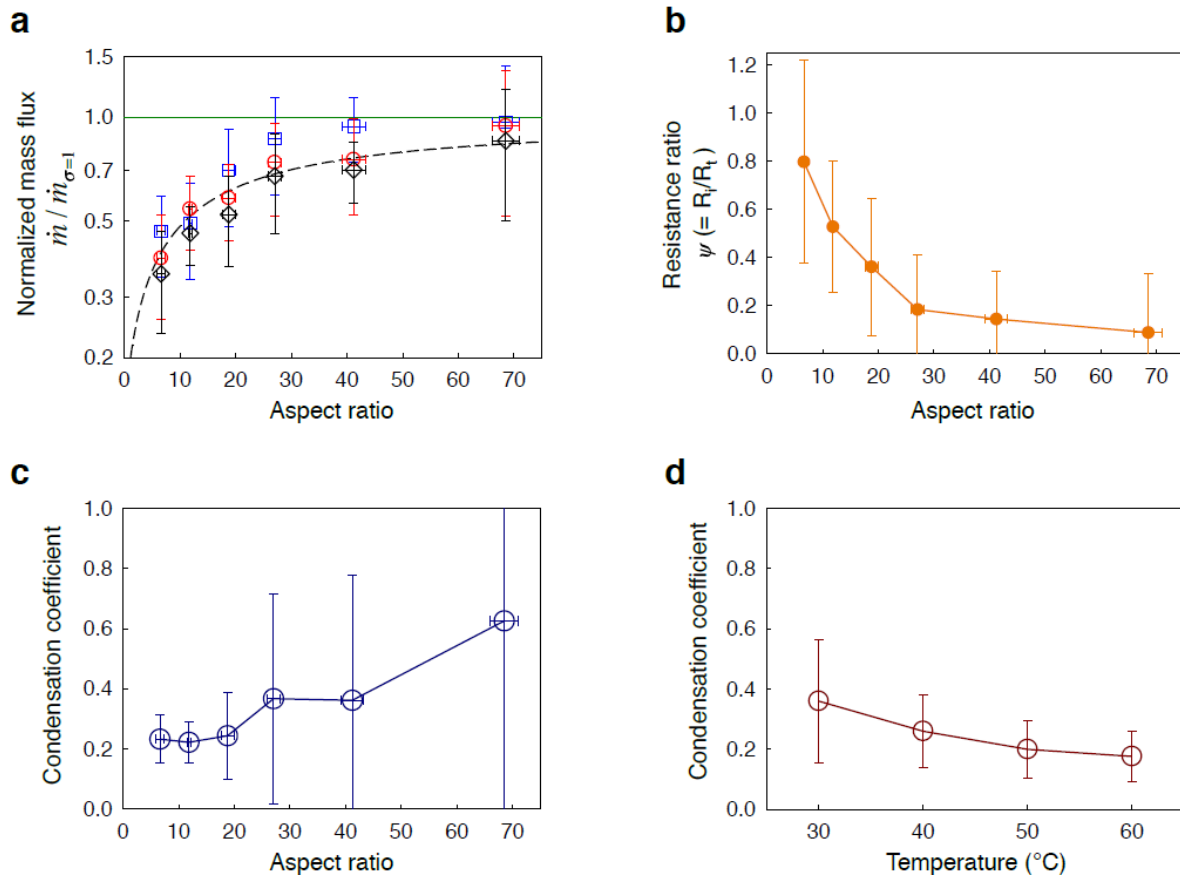
Figure 5. Regime of interface-governed transport and estimated condensation coefficients.

a, Mass flux normalized by the maximum mass flux corresponding to zero interfacial resistance ($R_i = 0$) for different concentrations of draw solution reveals a marked departure at smaller aspect ratios. Temperature is 39.0±0.3 °C. Green line indicates ideal normalized flux for $\sigma = 1$ as a guide for the eyes. Black dotted line denotes the theoretically predicted normalized mass flux for a condensation coefficient of 0.23. **b,** Ratio of interface resistance to transmission resistance for different AR at a temperature of 39.0±0.3 °C, obtained from data shown in panel **a**. **c, d** Estimated condensation coefficients for different AR at a temperature of 39.0±0.3 °C, obtained from data shown in panel **a** (**c**) and for different temperatures, obtained from flux measurements on membranes with AR of 9.6±0.7 (**d**). Vertical error bars in all panels represent uncertainty combining S.D. of data points and the effect of uncertainty in pressure inside the nanopores, p (See Supplementary Section 9). Each data point was obtained from measurements on 3 to 5 different membranes. Horizontal error bars in all panels represent ±S.D. for AR as described in Methods.